ACS NANO

www.acsnano.org

ARTICLE

Gestational Exposure to Black Phosphorus Nanoparticles Induces Placental Trophoblast Dysfunction by Triggering Reactive Oxygen Species-Regulated Mitophagy

Changqing Zhang, Li Xiao, Zhenya Fang, Shuxian Li, Chao Fan, Ruolan You, Chunying Wang, Anna Li, Xietong Wang,* and Meihua Zhang*

Cite This: *ACS Nano* 2025, 19, 16517−16533

Read Online

ACCESS | Metrics & More | Article Recommendations | Supporting Information

ABSTRACT: As a type of two-dimensional nanomaterial, black phosphorus (BP) has attracted considerable interest for applications in various fields. Despite its advantages, including biodegradability and biocompatibility, recent studies have shown that BP exhibits cytotoxicity in different types of cells. However, no studies have investigated the effects of BP exposure during pregnancy. Herein, we first investigated the effect of gestational exposure to BP nanoparticles (BPNPs) in a mouse model. Our findings indicated that BPNPs exposure restricted fetal growth and hindered placental development. In HTR8/SVneo trophoblast cells, BPNPs inhibited cell proliferation, migration, and invasion and caused apoptosis in a dose-dependent manner. Furthermore, BPNPs induced intracellular reactive oxygen species (ROS) overproduction and extensive mitochondrial damage. We further demonstrated that BPNPs promoted mitophagy via the PINK1/Parkin signaling pathway. Parkin siRNA knockdown rescued BPNPs-induced trophoblast dysfunction, while ROS inhibition attenuated BPNPs-induced cytotoxicity by reducing mitochondrial damage. Finally, treatment with mdivi-1, a mitophagy inhibitor, mitigated mitochondrial membrane potential reduction, excessive mtROS production, and the resulting trophoblast dysfunction. *In vivo* model investigation indicated that the application of mdivi-1 ameliorated embryonic resorption and fetal growth by alleviating placental damage. In summary, gestational exposure to BPNPs impairs fetal growth by inducing placental trophoblast dysfunction through ROS-regulated, PINK1/Parkin-dependent mitophagy.

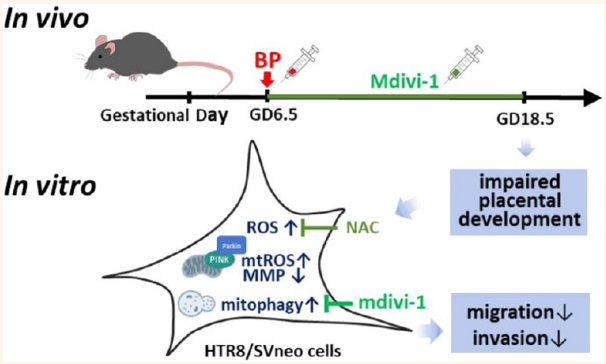

KEYWORDS: *black phosphorus, nanoparticles, placental trophoblast, mitophagy, ROS*

INTRODUCTION

Black phosphorus (BP), a recently discovered member of two-dimensional (2D) materials, has attracted considerable attention since its first exfoliation in 2014.[1] Compared with other 2D materials, BP possesses unique optical and electrical properties, making it a promising nanomaterial for applications in electronics, optoelectronics, and biosensors.[2−5] BP has also been extensively explored for biomedical applications owing to its excellent biodegradability and biocompatibility.[6] A considerable number of studies have investigated its use in photodynamic therapy (PDT) and photothermal therapy (PTT) for treating cancers, including breast cancer, cervical cancer, and glioma.[7,8] Moreover, BP is regarded as an excellent drug delivery vehicle. The widespread applications of BP across various fields will inevitably lead to excessive exposure, raising concerns regarding its potential toxicity. Previous studies have revealed that BP toxicity depends on its size and thickness and varies across different cell types.[9−11] A study on zebrafish demonstrated that BP exposure induces developmental defects, particularly cardiovascular dysfunction, indicating that BP poses a risk of developmental perturbations.[12]

The placenta, a key organ connecting the mother and fetus, plays a vital role in gas and nutrient exchange and growth

Received: December 25, 2024
Revised: April 14, 2025
Accepted: April 15, 2025
Published: April 23, 2025

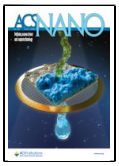

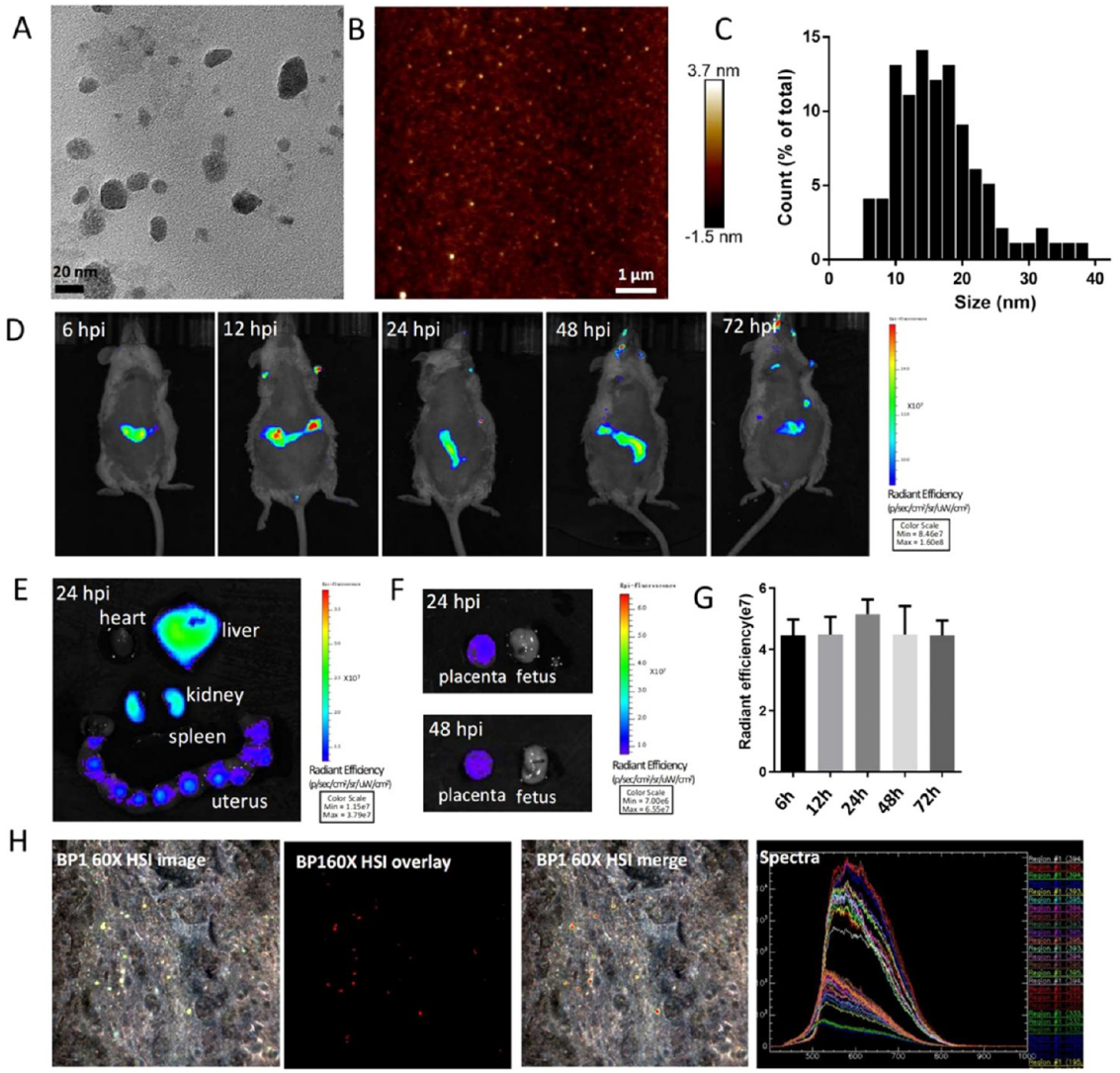

Figure 1. Characterization and biodistribution of BPNPs. (A) TEM image of BPNPs. (B) Representative AFM (atomic force microscope) morphology and (C) Statistic analysis of the lateral size of BPNPs. (D) Time-lapse fluorescence images of Cy5.5-labeled BPNPs in pregnant mice. (E) *Ex vivo* fluorescence images of the major organs from the BPNPs-treated mice at 24 h post injection (hpi). (F) *Ex vivo* fluorescence images of the placenta and fetus at 24 hpi and 48 hpi. (G) Fluorescence intensity of each placenta at different time intervals. (H) Hyperspectral imaging of BPNPs in mouse placenta tissues. From left to right: Hyperspectral image of placenta tissue, mapping of BPNPs, overlay image of the placenta tissue and BPNPs and the spectral library of BPNPs of selected regions.

factor and hormone secretion. The crucial functions of the placenta are largely mediated by trophoblast, which form the outer layer of the placenta.[13] Normal proliferation, invasion, and migration of trophoblast cells are essential for uterine spiral artery remodeling.[14] Dysfunctional trophoblast cells contribute to adverse pregnancy outcomes, including preterm birth, miscarriage, and fetal growth restriction. Previous studies have shown that the developing fetus is particularly vulnerable to environmental pollutants. Prenatal exposure to environmental chemicals and psychosocial stressors may lead to placental dysfunction and pregnancy complications.

Mitophagy is a form of intracellular autophagy that selectively degrades damaged or nonfunctioning mitochondria.[15] It is initiated by the stabilization of PINK1 (PTEN_induced kinase 1) on the surface of damaged mitochondria, which subsequently recruits and activates Parkin. Parkin, an E3 ubiquitin ligase, amplifies the mitophagy signal by further ubiquitinating mitochondrial proteins on the outer layer. Mitophagy plays a crucial role in maintaining mitochondrial quality control and regulating mitochondrial quantity in response to environmental stress. However, excessive mitophagy can lead to placental dysplasia.[16,17] Studies have shown that placental mitochondrial function adapts to environmental cues over the course of gestation to support fetal growth.[18] A few studies on mice have demonstrated that mitophagy can be overactivated by the heavy metal cadmium in placental trophoblast, impairing placental function and leading to fetal growth restriction.[19−22] To the best of our knowledge, the role of mitophagy in BP-induced cytotoxicity is yet to be clarified.

Based on previous studies, we speculate that gestational exposure to BP may affect fetal development by disrupting placental trophoblast function through mitochondrial damage. To test this hypothesis, we investigated the effects of BPNPs exposure on the function of placenta and trophoblast cells. First, we established a murine *in vivo* model of BPNPs exposure during pregnancy and confirmed its toxic effects on fetal growth and placentation. Then, *in vitro* experiments

https://doi.org/10.1021/acsnano.4c18731
ACS Nano 2025, 19, 16517−16533

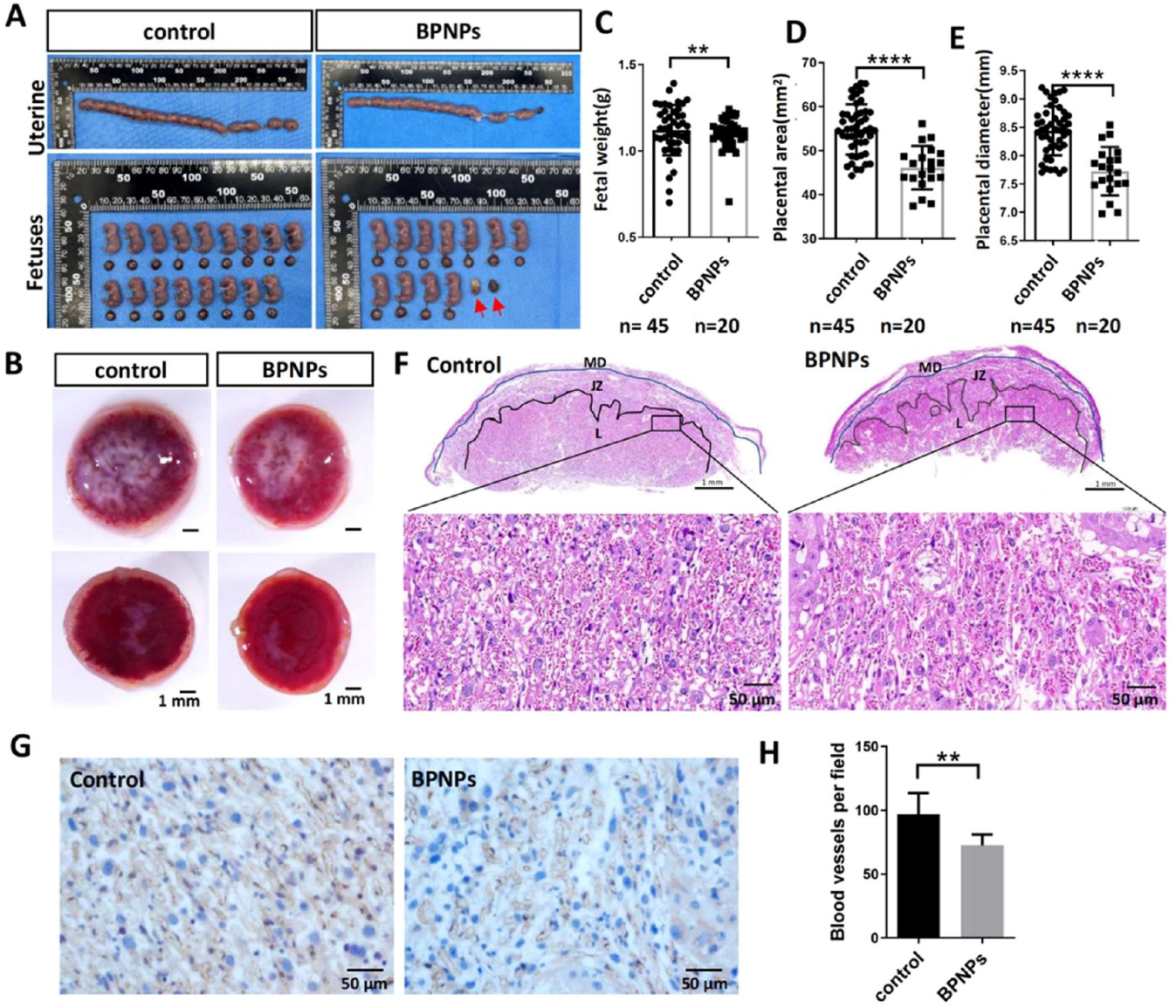

Figure 2. Effects of BPNPs exposure on pregnancy in mice. (A) The uterine and fetus appearance in control and BPNPs-exposed mice on GD18.5. Red arrow indicates embryo absorption. (B) Representative images of the mouse placenta. (C–E) Quantitative analysis of the fetus weight, placenta area and diameter. (F) HE staining of placenta tissue on GD18.5 under light microscope. MD: Maternal decidual, JZ: Junctional zone, L: Labyrinth. (G) Immunohistochemistry of placental CD31 expression. Representative images were chosen from placental labyrinth. (H) Number of CD31-positive vessels. (n = 6 per group).

showed that BPNPs exposure inhibited trophoblast proliferation and impaired its function. We further demonstrated that BPNPs induced excessive reactive oxygen species (ROS) production and extensive mitochondrial damage. Next, to elucidate the underlying molecular mechanism, RNA sequencing was performed, revealing that mitophagy played a key role in BPNPs-induced cytotoxicity in human trophoblast. Finally, the inhibition of mitophagy abolished BPNPs-induced adverse pregnancy outcomes and rescued trophoblast dysfunction. Our study provides essential insights for the safer use of BP-based nanomaterials and enables better understanding of the toxic effects of nanoparticles exposure to the reproductive system.

RESULTS

Characterization of BPNPs and *In Vivo* Biodistribution Analysis. To obtain a comprehensive understanding of the microscopic structure of BPNPs, we first characterized the morphology and lateral size using transmission electron microscopy (TEM). As shown in Figure 1A, exfoliated BP exhibited excellent dispersion in an aqueous solution without measurable aggregation. Quantitative analysis of approximately 100 nanoparticles revealed a lateral size ranging from 5.7 to 38.4 nm, with approximately 13% measuring smaller than 10 nm and over 75% falling within 10–30 nm. The average diameter of BPNPs was determined to be 16.52 ± 6.59 nm. Moreover, the average thickness was 2 nm, corresponding to a stack of three crystalline unit layers (Figure 1B,C). To track the biodistribution of BPNPs *in vivo*, nanoparticles were fluorescently labeled with a near-infrared dye (Cy5.5). Following intravenous administration of Cy5.5-BPNPs to pregnant mice at GD12.5, longitudinal tissue distribution was monitored using an IVIS Spectrum system. Fluorescence signal was observed in uterus at 6 h postinjection, peaking at 24 h, followed by gradual clearance after 48 h (Figure 1D–G).

https://doi.org/10.1021/acsnano.4c18731
ACS Nano 2025, 19, 16517–16533

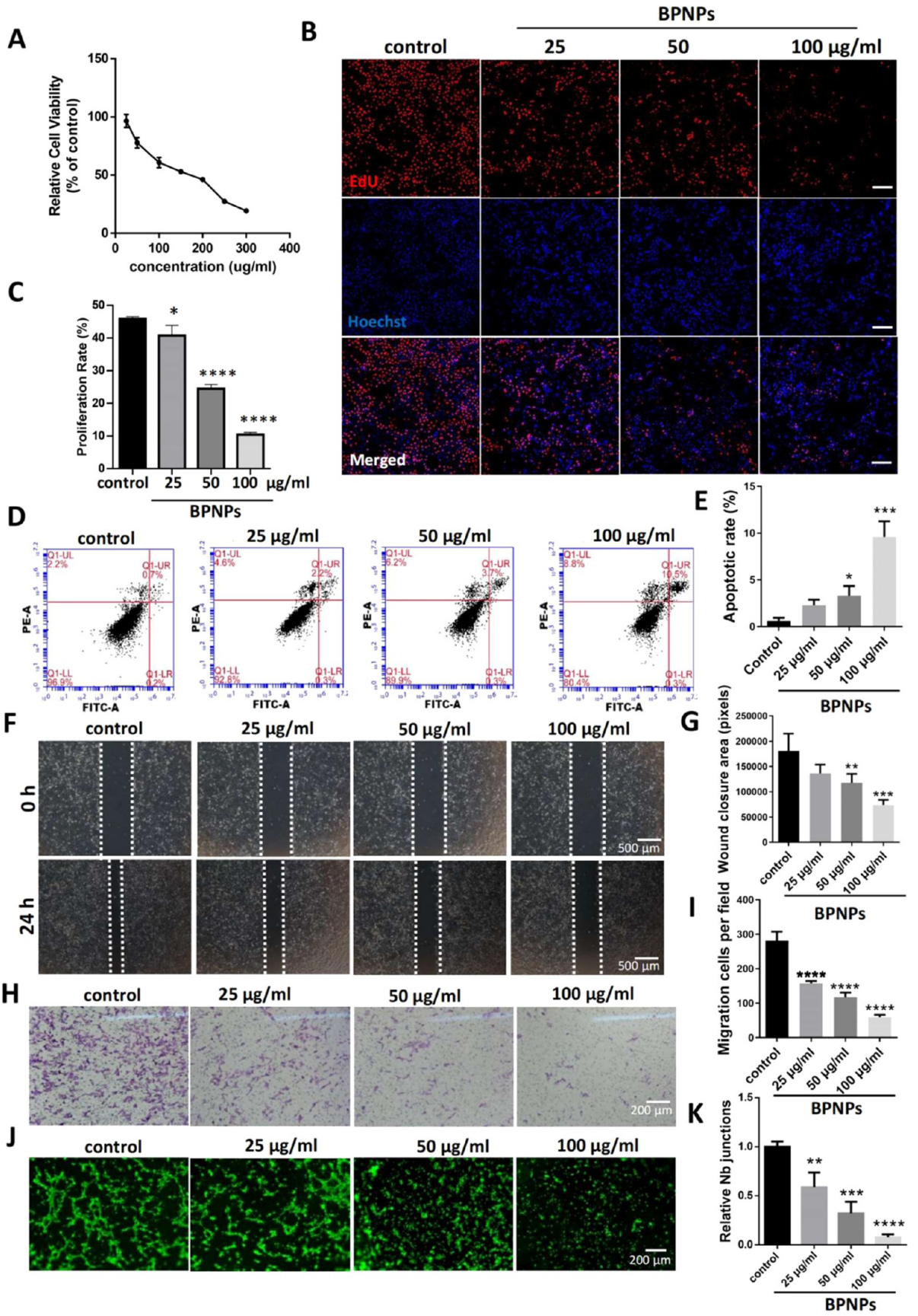

Figure 3. Cytotoxicity of BPNPs exposure in HTR8 cells. (A) Cell viability was evaluated by the CCK8 assay in trophoblast cells treated with different concentrations of BPNPs for 24 h. (B) Proliferating trophoblast cells were detected using the EdU incorporation method. Scale bar: 200 μm. (C) Quantitative analysis of the EdU$^+$ cells. (D, E) Apoptosis of HTR8 cells was analyzed using the Annexin V/PI method by flow cytometry. (F) Representative images of the wound healing assay of HTR8 cells at 0 and 24 h following treatment with different

https://doi.org/10.1021/acsnano.4c18731
ACS Nano 2025, 19, 16517−16533

Figure 3. continued

concentrations of BPNPs. (G) Quantitative analysis of the wound closure rate. (H) Representative images of the Transwell assay of HTR8 cells following treatment with different concentrations of BPNPs. (I) Quantitative analysis of invaded HTR8 cells in five randomly selected fields. (J) Representative images of the tube formation assay of HTR8 cells following treatment with different concentrations of BPNPs. (K) Quantitative analysis of the number of branch nodes junctions of HTR8 cells following treatment with different concentrations of BPNPs.

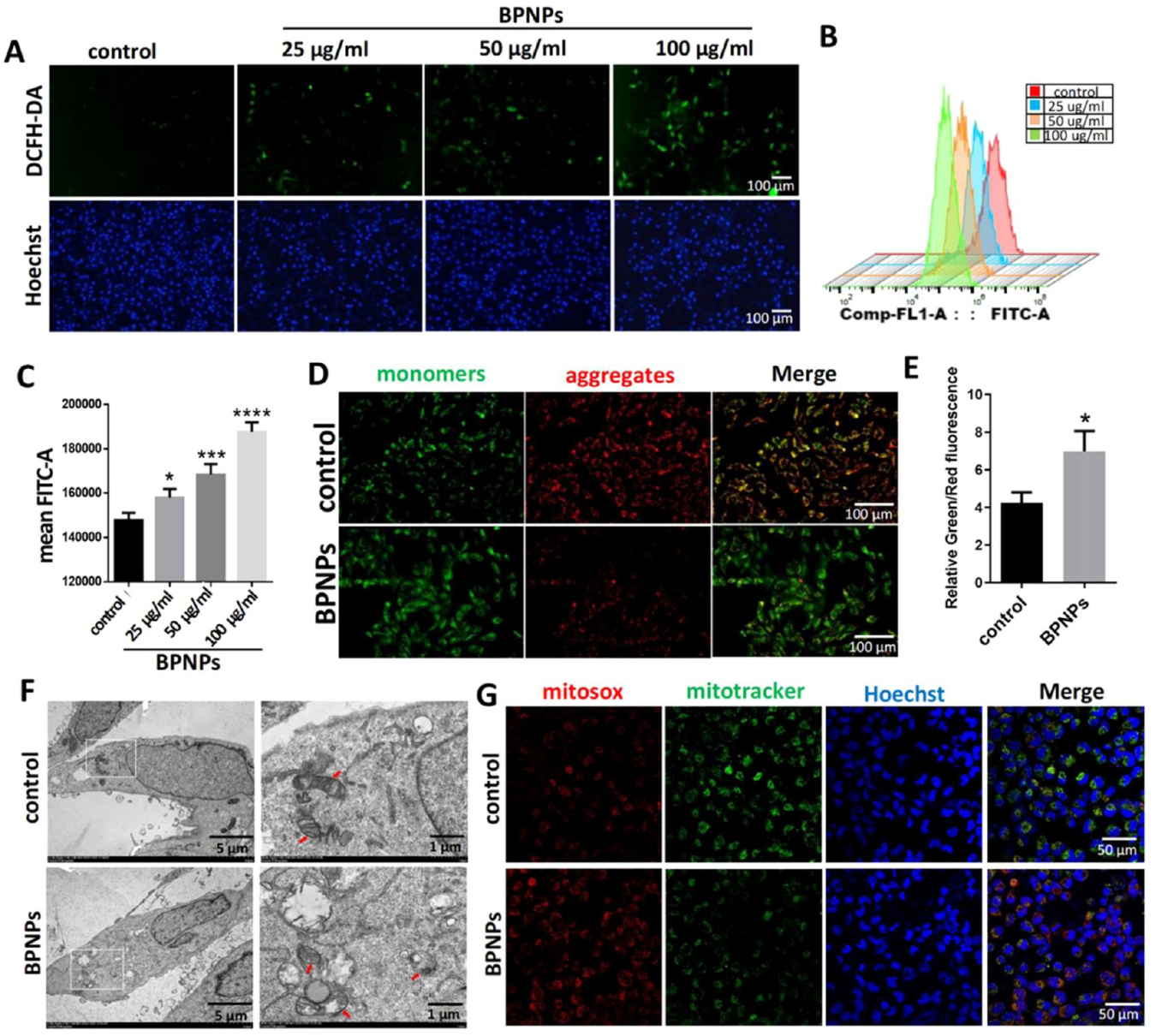

Figure 4. Effects of BPNPs on intracellular ROS levels and mitochondria. (A) Fluorescence image of intracellular ROS detected by the DCFH-DA probe (green). The nuclei were stained with Hoechst (blue). Cells were treated with BPNPs for 24 h prior to detection. (B, C) Intracellular ROS levels in HTR8 cells detected by flow cytometry. The mean levels of FITC fluorescence intensity were quantified. (D) Fluorescence images of mitochondrial membrane potential staining in HTR8 cells using the JC-1 probe. At high MMP, JC-1 forms aggregates that emit red fluorescence in mitochondrial matrix. At low MMP, JC-1 forms monomers that emit green fluorescence in cytoplasm. (E) Relative green/red fluorescence intensity ratio in each group. (F) TEM images of trophoblast cells in control and BPNPs-exposed groups. Red arrow indicated mitochondrial vacuolization and mitochondrial ridge breaks. (G) Detection of mitochondrial ROS using Mitosox-red.

Consistent with previous studies,[23−26] BPNPs were absent in heart while accumulating in the liver and kidney (Figure 1E). The uptake of BPNPs in the placenta was further confirmed by the CytoViva Nano-Scale Hyperspectral Microscope Imaging System. Enhanced dark-field hyperspectral imaging of placental sections identified abundant BPNPs within the placenta, appearing as small discrete dots (Figure 1H). Particularly, Cy5.5 fluorescence was exclusively localized in placental tissue with undetectable signal in the fetus (Figure 1F), implying potential placenta-mediated modulation of fetal development rather than direct embryonic exposure.

https://doi.org/10.1021/acsnano.4c18731
ACS Nano 2025, 19, 16517−16533

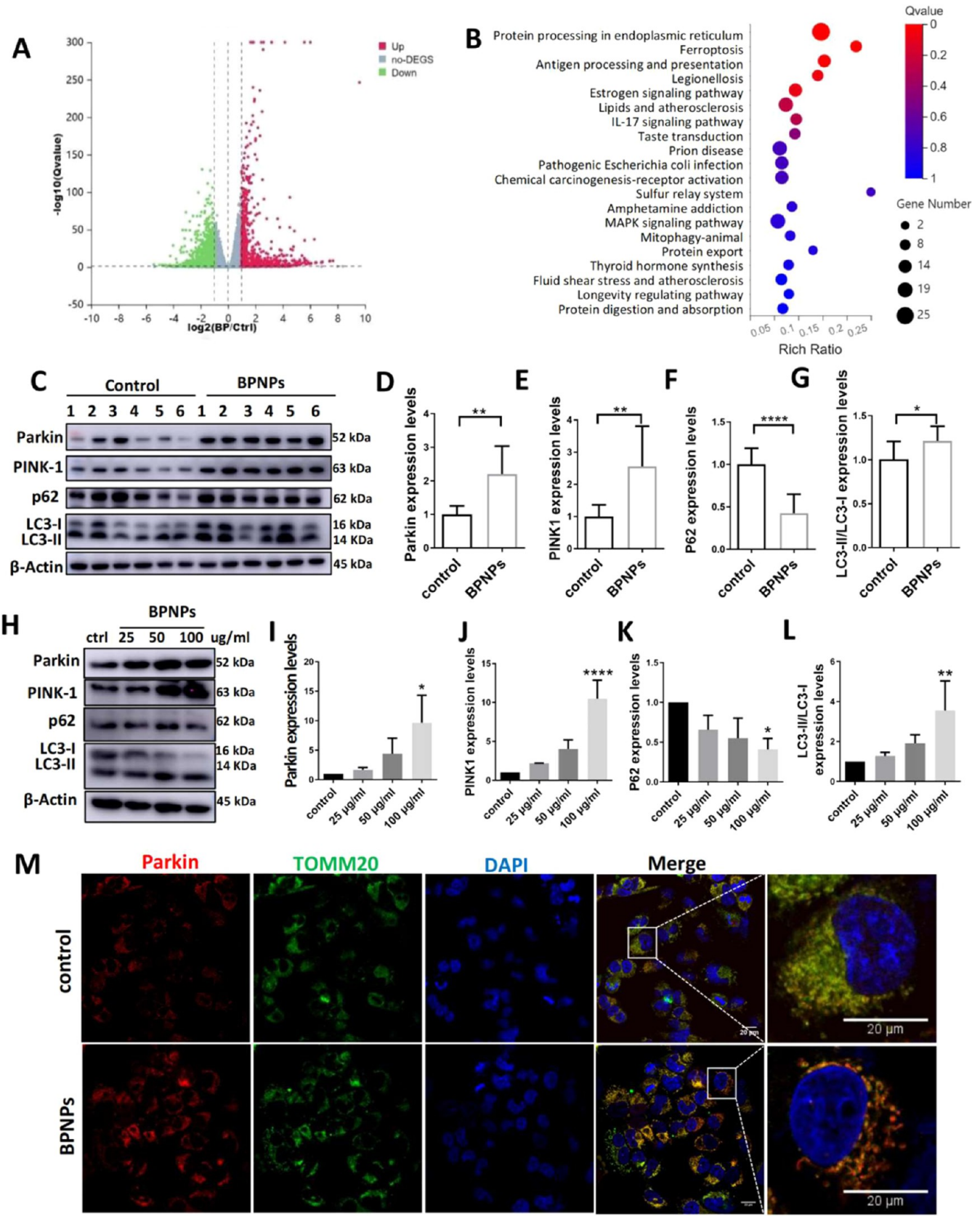

Figure 5. BPNPs activated mitophagy *via* the PINK1/Parkin signaling pathway. (A) Volcano plot of the distribution of all differentially expressed genes between control and BPNPs-exposed group. (B) Top 20 KEGG pathway enrichment of the DEGs. Reprinted from doi: 10.1016/j.tox.2024.153810 with permission from Elsevier. (C, H) Expression of mitophagy-related proteins Parkin, PINK1, P62, LC3 in mice placenta (C) and human HTR8 cells (H) using Western blotting following treatment with BPNPs. (D−G) and (I−L) Quantification of the expression of mitophagy-related proteins presented in (C, H). (M) Immunofluorescence of Parkin and TOMM20 in trophoblast cells.

https://doi.org/10.1021/acsnano.4c18731
ACS Nano 2025, 19, 16517−16533

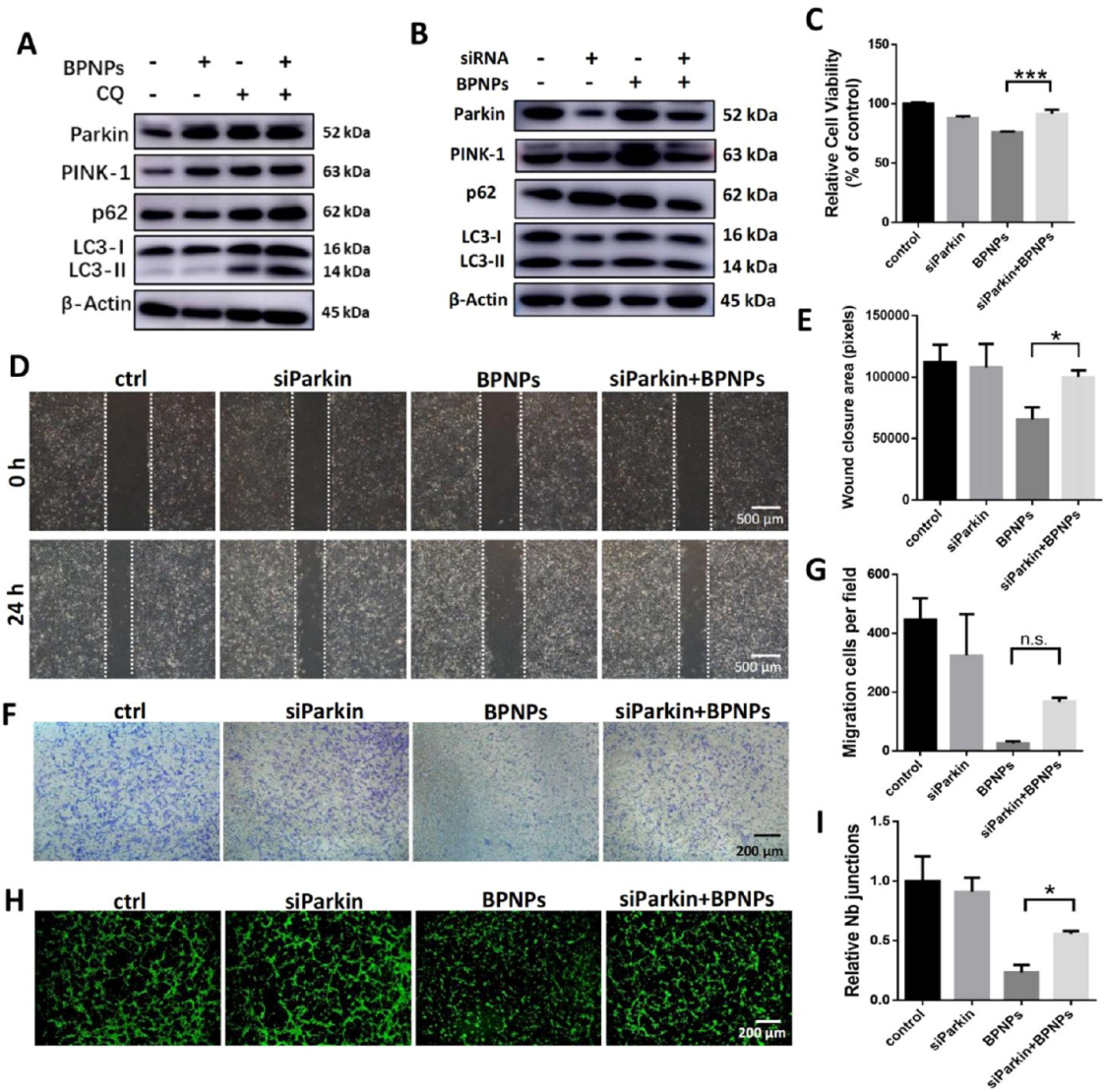

Figure 6. Parkin knockdown rescued the BPNPs-induced trophoblast cell dysfunction. (A-B) Expression of mitophagy-related proteins by Western blotting. (C) CCK8 assay of the trophoblast cells treated with BPNPs and Parkin siRNA. (D) Representative images of the wound healing assay of HTR8 cells at 0 and 24 h following treatment with BPNPs and Parkin siRNA. (E) Quantitative analysis of the wound closure rate. (F) Representative images of the Transwell assay of HTR8 cells following treatment with BPNPs and Parkin siRNA. (G) Quantitative analysis of the invaded HTR8 cells. (H) Representative images of the tube formation assay of HTR8 cells following treatment with BPNPs and Parkin siRNA. (I) Quantitative analysis of the number of branch nodes junctions of HTR8 cells following treatment with BPNPs and Parkin siRNA.

Effects of BPNPs Exposure on Placental Development. The effect of gestational exposure to BPNPs was first evaluated in a murine model. Pregnant mice were intravenously injected with BPNPs at 5 mg/kg on GD6.5. On GD18.5, the mice were euthanized for analysis (Figure 2A,B). We found that BPNPs exposure increased embryo absorption rate (5/39 in total). Fetal weight, as well as placental diameter and area, significantly decreased in BPNPs-treated mice (Figure 2C−E), indicating that BPNPs restricted fetal growth by hindering placental development. Histological examination of the placenta revealed that cells in the control group were well differentiated, and arranged. Blood sinuses were abundant. By contrast, the placental cells in the BPNPs-treated group were disorganized, with larger intercellular gaps (Figure 2G). Notably, no observable tissue damage was detected in other major organs (including the heart, liver, spleen, and kidneys) (Figure S1). Furthermore, CD31-positive blood vessels were significantly reduced in the placental labyrinth of BPNPs-treated mice (Figure 2G). Quantitative analysis indicated that the placental blood vessel density decreased following BPNPs exposure (Figure 2H). These results indicate that prenatal exposure to BPNPs during the first trimester had adverse effects on placental development.

BPNPs Exposure Causes Placental Trophoblast Dysfunction. To evaluate the cytotoxicity of BPNPs, the human trophoblast cell line HTR8/SVneo (HTR8) was treated with different concentrations of BPNPs for 24 h. The CCK8 assay demonstrated that BPNPs exposure reduced cell viability in a dose-dependent manner (Figure 3A). In support of this, proliferating cells labeled with EdU decreased as well (Figure 3B,C). Moreover, cell apoptosis was assessed using the Annexin V/propidium iodide (PI) assay, which revealed a substantial increase in Annexin V−positive HTR8 cells following BPNPs treatment (Figure 3D,E). To further evaluate

https://doi.org/10.1021/acsnano.4c18731
ACS Nano 2025, 19, 16517−16533

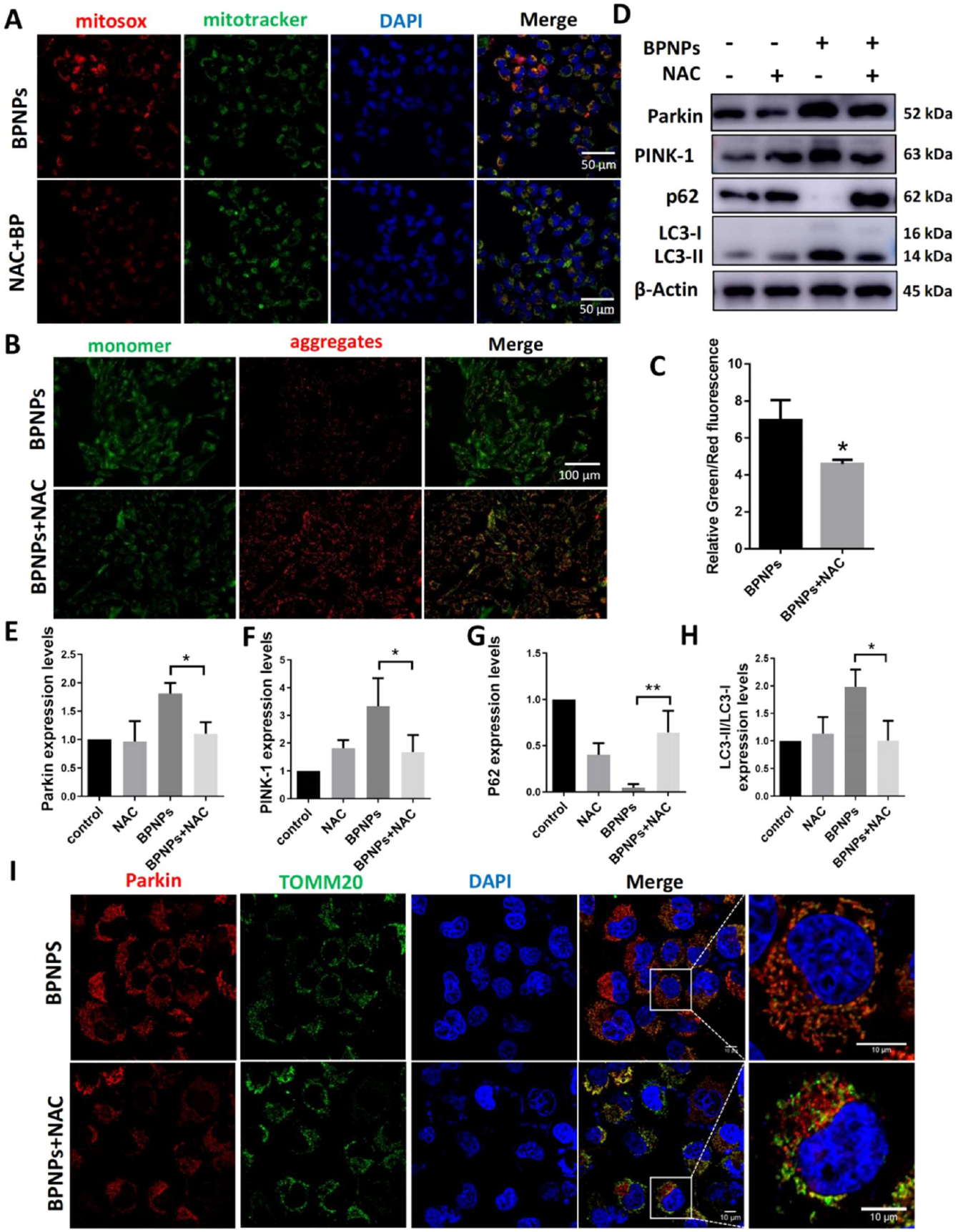

Figure 7. Inhibition of intracellular ROS by NAC mitigated BPNPs-caused mitochondrial damage by suppression of mitophagy. (A) Detection of mitochondrial ROS using Mitosox-red upon BPNPs and NAC cotreatment. (B) Fluorescence images of mitochondrial membrane potential in HTR8 cells following NAC and BPNPs treatment. (C) Relative green/red fluorescence intensity ratio of JC-1 staining. (D) Expression of mitophagy-associated proteins Parkin, PINK1, P62, LC3 in human trophoblast cells. (E−H) Quantification of

https://doi.org/10.1021/acsnano.4c18731
ACS Nano 2025, 19, 16517−16533

Figure 7. continued

the expression of mitophagy-associated proteins presented in (D). (I) Immunofluorescence of Parkin and TOMM20 in trophoblast cells following BPNPs and NAC cotreatment.

the effects of BPNPs on trophoblast function, wound healing, transwell, and tube formation assays were performed. As shown in Figure 3F, the wound closure rate was significantly decreased in BPNPs-treated group, indicating that the migratory ability of HTR8 cells was markedly reduced upon BPNPs exposure (Figure 3G). Consistently, BPNPs treatment decreased the number of invaded HTR8 cells in the Transwell assay (Figures 3H,I). Furthermore, the vasculogenic capacity of trophoblasts was impaired by BPNPs treatment (Figure 3J,K). These results indicate that BPNPs exposure inhibited trophoblast proliferation, promoted apoptosis, and impaired the function of placental trophoblasts.

BPNPs Exposure Induces Mitochondrial Damage in Trophoblast Cells. Previous studies have shown that oxidative stress is closely associated with BP-induced cytotoxicity. To investigate its role in trophoblast cells, intracellular ROS was detected using a fluorescent probe DCFH-DA. Fluorescence microscopy revealed a gradual increase in green fluorescence following BPNPs exposure (Figure 4A). ROS levels were further quantified *via* flow cytometry after DCFH-DA staining, which indicated that BPNPs exposure enhanced ROS production (Figure 4B). To assess the redox state in the mouse placenta, we measured the levels of superoxide dismutase (SOD) and malondialdehyde (MDA). While SOD activity decreased, MDA level was increased in BPNPs-treated placentas, indicating that BPNPs disrupted the redox balance in mouse placenta (Figure S2). As mitochondria are the primary source of intracellular ROS production, we hypothesized that mitochondrial damage was induced alongside excessive ROS production. Mitochondrial membrane potential (MMP) was measured using the JC-1 probe, which forms aggregates that emit red fluorescence at high MMP and monomers that emit green fluorescence at low MMP. As shown in Figure 4D, red fluorescence was diminished, while green fluorescence was elevated in BPNPs-exposed cells. The ratio of green to red fluorescence was significantly increased (Figure 4E), indicating a decrease in MMP following BPNPs exposure. Furthermore, TEM imaging revealed an accumulation of fragmented mitochondria in BPNPs-treated trophoblast cells, confirming mitochondrial damage (Figure 4F). Finally, mitochondrial ROS levels were assessed using MitoSOX Red staining, which exhibited a considerable increase in mitochondrial ROS levels upon BPNPs exposure (Figure 4G). Taken together, these results indicate that BPNPs induce oxidative stress and mitochondrial damage by increasing mitochondrial ROS levels in trophoblast cells.

BPNPs Exposure Provokes Mitophagy *via* the PINK1/Parkin Signaling Pathway in Trophoblast Cells. To investigate the molecular mechanism of BPNPs-induced cytotoxicity in trophoblast, high-throughput RNA sequencing (RNA-seq) analysis was performed on HTR8 cells from control and BPNPs-treated groups. Differentially expressed genes (DEGs) with 2-fold or more changes between BPNPs and the control group were differentiated using an adjusted p value threshold of ≤ 0.05. A total of 1948 DEGs were detected, of which 1182 were downregulated and 766 were upregulated (Figure 5A). Among the upregulated DEGs, KEGG pathway analysis revealed mitophagy was prominently enriched (Figure 5B). Considering that previous studies have indicated a role of autophagy in the BPNPs-induced cytotoxicity and that mitochondrial damage was observed herein, we focused on mitophagy for further analysis. To evaluate whether BPNPs exposure triggered mitophagy, we examined the expression of mitophagy markers in mouse placenta. As shown in Figure 5C, BPNPs treatment increased LC3 protein levels while decreasing P62 levels, indicating that BPNPs treatment promoted autophagy induction without blocking autophagic flux. Meanwhile, the levels of Parkin and PINK1 were also significantly increased by BPNPs exposure, indicating that mitophagy was provoked (Figure 5C−G). To further validate these findings, we assessed mitophagy marker expression in HTR8 trophoblast cells. Consistently, BPNPs exposure led to a dose-dependent increase in Parkin, PINK1, and LC3 expression while reducing P62 levels (Figure 5H−L). Moreover, immunofluorescence staining revealed that BPNPs exposure promoted the colocalization of TOMM20 and Parkin in both trophoblast cells (Figure 5M) and mouse placenta (Figure S3), indicating that Parkin was translocated to mitochondria in BPNPs-treated trophoblasts.

To further confirm the role of Parkin-mediated mitophagy, we first applied chloroquine (CQ) to assess autophagic flux following BPNPs exposure. As expected, CQ treatment considerably increased LC3-II/I and P62 expression, indicating autophagy inhibition. Compared to the BPNPs-treated group, the combination of BPNPs and CQ further elevated LC3-II/I and P62 levels, along with an increase in Parkin expression (Figure 6A). Next, we used siRNA targeting Parkin in HTR8 cells to evaluate its role in BPNPs-induced cytotoxicity. As expected, Parkin siRNA effectively reduced Parkin protein levels (Figure 6B). The BPNPs-caused impairment of trophoblast cell viability, invasion, and migration was reversed by Parkin siRNA (Figure 6C−G). Moreover, the vasculogenic capacity of trophoblast cells was mitigated by Parkin knockdown (Figure 6H,I). Collectively, these results indicated that gestational exposure to BPNPs invoked Parkin-mediated mitophagy in placental trophoblasts.

BPNPs Induce Mitophagy *via* Increasing ROS Production in Trophoblast Cells. To identify the upstream regulatory pathway, HTR8 cells were pretreated with *N*-acetyl-L-cysteine (NAC), a commonly used ROS inhibitor. First, mitochondrial ROS levels were considerably reduced in trophoblast cells cotreated with BPNPs and NAC compared to the BPNPs group (Figure 7A). JC-1 probe staining further demonstrated that NAC treatment mitigated BPNPs-induced mitochondrial damage, as indicated by the preservation of MMP (Figure 7B,C). Next, we examined the expression of mitophagy-related proteins. As shown in Figure 7D, NAC treatment considerably decreased the expression of PINK1, Parkin, and LC3-II while increasing P62 levels in the NAC +BPNPs group (Figure 7E−H). Notably, Parkin mitochondrial translocation was also suppressed, as evidenced by reduced colocalization of Parkin and TOMM20 (Figure 7I). Finally, as expected, NAC treatment alleviated BPNPs-induced impairments in trophoblast cell invasion and migration (Figure S4).

https://doi.org/10.1021/acsnano.4c18731
ACS Nano 2025, 19, 16517−16533

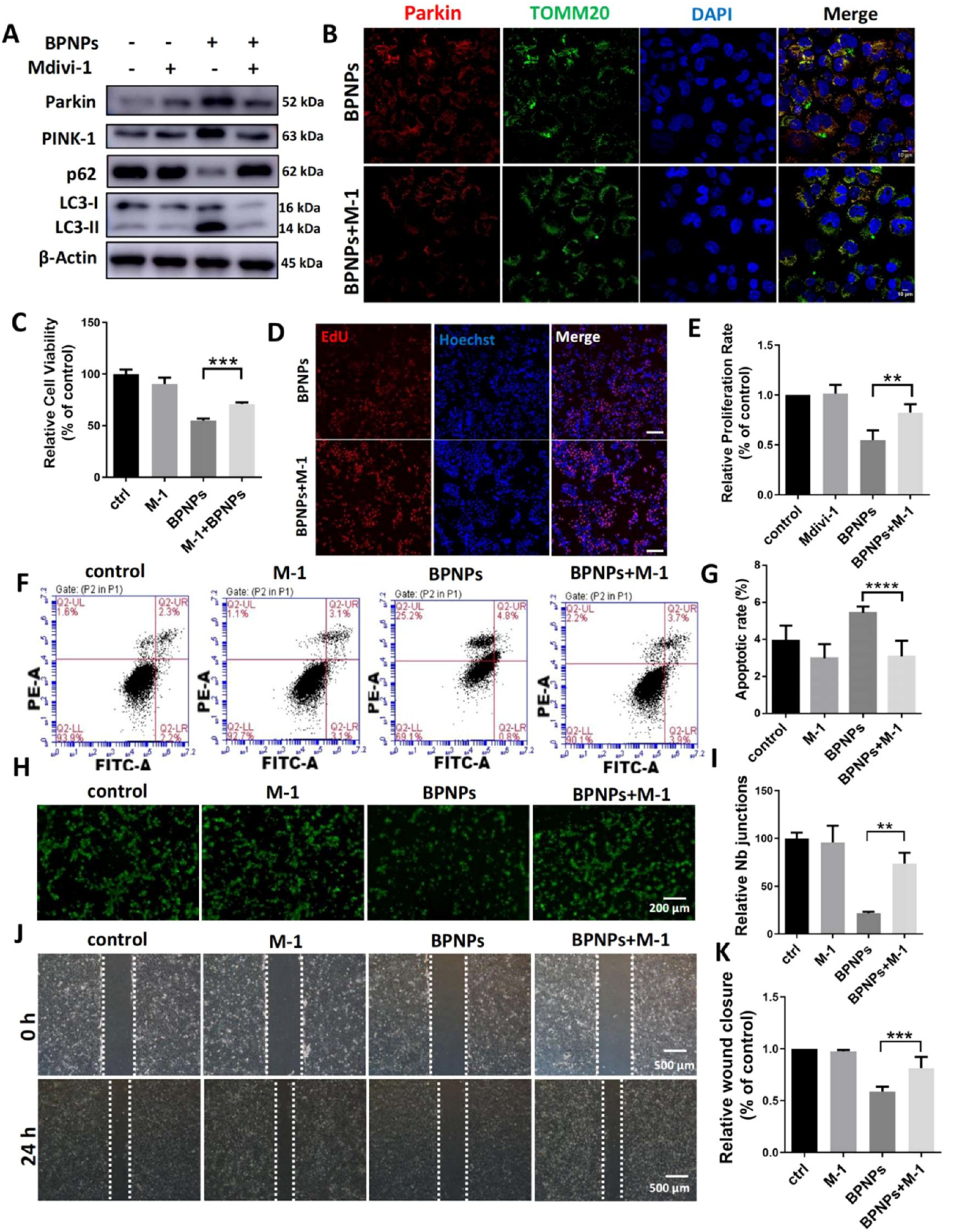

Figure 8. Mdivi-1 protects against BPNPs-induced cell dysfunction *via* blocking mitophagy in trophoblast. (A) Expression of mitophagy-associated proteins Parkin, PINK1, P62, LC3 in trophoblast cells. (B) Immunofluorescence of Parkin and TOMM20 in trophoblast cells. Scale bar: 10 μm. (C) Cell viability was evaluated by the CCK8 assay in trophoblast cells. (D) Detection of proliferating trophoblast cells using the EdU incorporation method. (E) Quantitative analysis of the EdU^+ cells. (F) Apoptosis of HTR8 cells was analyzed using the

https://doi.org/10.1021/acsnano.4c18731
ACS Nano 2025, 19, 16517−16533

Figure 8. continued

Annexin V/PI method by flow cytometry. (G) Quantitative analysis of the apoptotic cells. (H) Representative images of the tube formation assay of HTR8 cells following treatment with BPNPs and mdivi-1. (I) Quantitative analysis of the number of branch nodes junctions of HTR8 cells following treatment with BPNPs and mdivi-1. (J) Representative images of the wound healing assay of HTR8 cells at 0 and 24 h following treatment with BPNPs and mdivi-1. (K) Quantitative analysis of the wound closure rate.

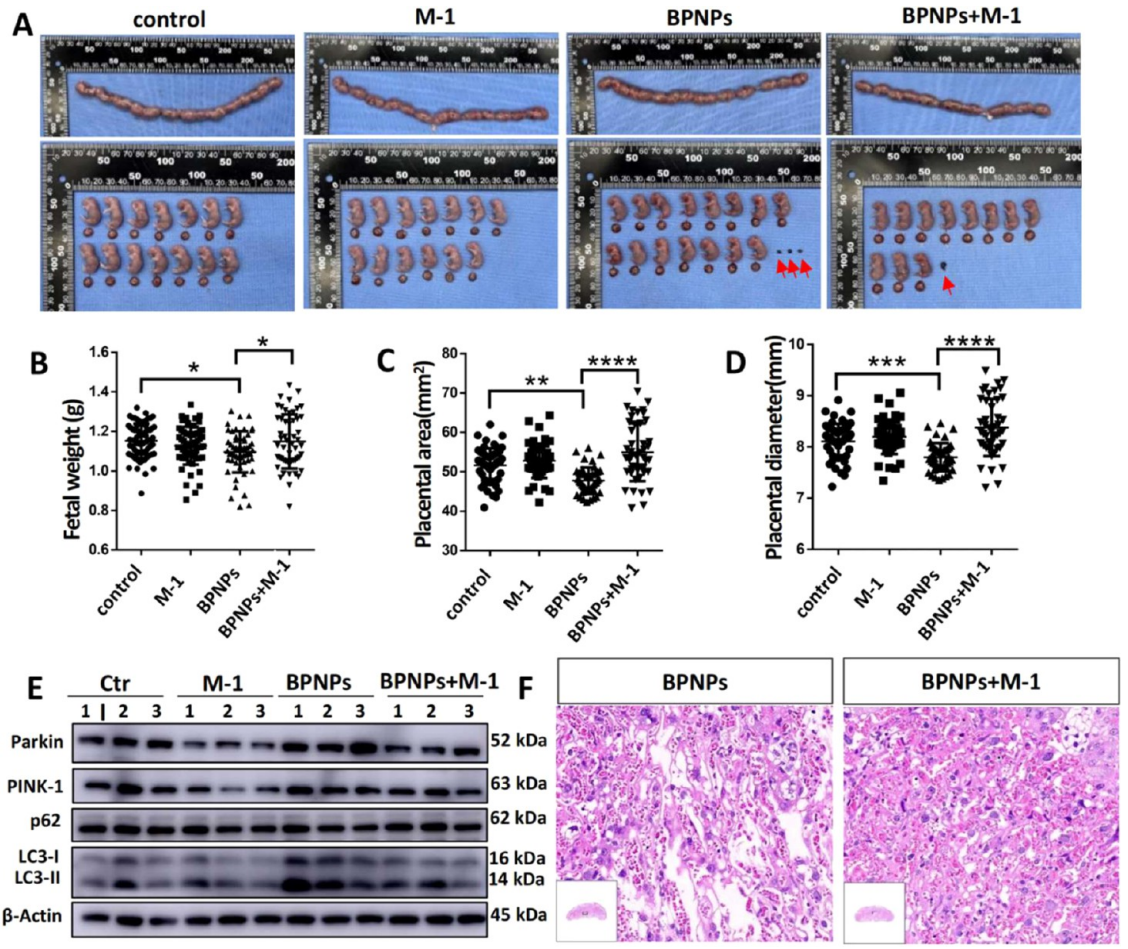

Figure 9. Mdivi-1 improves the BPNPs-induced adverse pregnancy outcomes in mice. (A) The uterine and fetus appearance on GD18.5 following treatment of BPNPs and mdivi-1. Red arrow indicates embryo absorption. (B–D) Quantitative analysis of the fetus weight, placenta area and diameter. (E) Expression of mitophagy-associated proteins Parkin, PINK1, P62, LC3 in mouse placenta. (F) Representative HE staining images from the placental labyrinth in BPNPs and BPNPs+mdivi-1 treated groups.

Inhibition of Mitophagy Alleviates the Cytotoxicity of BPNPs Exposure. To further investigate the role of mitophagy activation in BPNPs-induced cytotoxicity, mdivi-1, an inhibitor of Parkin mitochondrial translocation, was used in HTR8 trophoblast cells. HTR8 cells were treated with BPNPs in the absence or presence of mdivi-1 for 24 h. Western blot analysis revealed that mdivi-1 treatment reduced the expression levels of Parkin and PINK1 (Figure 8A). Moreover, Parkin mitochondrial translocation was effectively blocked (Figure 8B). As expected, mdivi-1 pretreatment significantly mitigated BPNPs-induced reductions in cell viability and proliferation in HTR8 cells (Figure 8C-E). Furthermore, BPNPs-induced apoptosis was attenuated by mdivi-1 pretreatment (Figure 8 F-G). The impaired vasculogenic and migratory abilities of HTR8 cells were also restored upon mdivi-1 treatment (Figure 8H-K). More importantly, mdivi-1 alleviated BPNPs-induced mitochondrial damage, as evidenced by increased MMP (JC-1 staining) and reduced mitochondrial ROS levels, specifically superoxide anion production (Figure S5).

To further confirm the role of mitophagy activation, mdivi-1 was administered to pregnant mice from GD6.5 to GD18.5. Mdivi-1 treatment effectively rescued BPNPs-induced reductions in fetal weight, placental diameter, and placental area (Figure 9A–D). The embryo absorption rate decreased to 3/46 (6.5%) following mdivi-1 administration. Consistently, mdivi-1 treatment reduced Parkin expression in the mouse placenta (Figure 9E). Histological analysis further confirmed that mdivi-1 alleviated BPNPs-induced cytotoxicity in the placenta (Figure 9F). Taken together, these findings strongly indicate that Parkin-mediated mitophagy plays a vital role in BPNPs-induced cytotoxicity in placental trophoblasts.

DISCUSSION

The rapid advancement of BP-based nanomaterial applications across various fields will inevitably lead to environmental

https://doi.org/10.1021/acsnano.4c18731
ACS Nano 2025, 19, 16517–16533

leakage, increasing the risk of human exposure. While several studies have investigated the toxicity of BP nanomaterials, most have been conducted using *in vitro* models. Early studies reported no substantial cytotoxicity of BP in various cell lines, including A549 (human lung carcinoma), HeLa (human cervical cancer), B16 (mouse melanoma), 4T1 (mouse breast cancer), and L929 (mouse fibroblast) cells, even at high concentrations up to 200 μg/mL.[27−30] However, contradictory findings were observed in another study, where BP exhibited toxic effects on A549 cells at concentrations above 100 μg/mL.[28] These inconsistencies may be attributed to variations in BP nanomaterial properties. Further studies have demonstrated that BP cytotoxicity is influenced by concentration, exposure duration, nanoparticle size, and cell type. Notably, BP with larger lateral size and thickness exhibits higher cytotoxicity, and different cell types show varying sensitivity to BP-induced toxicity—differing by more than 30-fold in some cases. These considerations highlight the need for our current study.

Moreover, BP toxicity has been demonstrated in some organoid models.[31] By contrast, the *in vivo* toxicity of BP remains less explored, with most studies conducted on mice. In most of these studies, mice typically received a single intravenous injection of BP. While some reports found no considerable organ damage or histological abnormalities following BP exposure,[27,32,33] others observed damage to the liver and kidneys.[34,35] Sun et al. reported that a single injection of BP nanosheets did not cause toxicity in mice, whereas multiple injections led to adverse effects on liver and renal function. Across these studies, the administered BP dose ranged from 2.5 to 50 mg/kg.[32,34] As BP is a new type of 2D nanomaterial, no data on human exposure doses are currently available. In such cases, some studies determine exposure concentrations based on the maximum tolerated dose, defined as the dose causing less than 15% body weight loss.[23] While a single BP injection at 5 mg/kg does not induce substantial organ damage,[32] higher doses of 20 or 30 mg/kg have induced toxic effects in mice.[35,36] Considering that pregnant women are more sensitive to chemical exposure, we administered BPNPs to pregnant mice *via* intravenous injection at a dose of 5 mg/kg, which is slightly lower than those used in previous studies.[36] The gestational stage was selected based on prior research,[37] because the first trimester is a critical period for trophoblast proliferation, differentiation, and migration. Surprisingly, BPNPs exposure resulted in considerable fetal growth restrictions and placental developmental abnormalities.

As for the molecular mechanism, many of the aforementioned studies have shown that ROS-mediated oxidative stress plays a dominant role in BP toxicity. For example, Song et al. found that layered BP induces apoptosis and necrosis through transient oxidative stress in fibroblastic cells.[9] Sun et al. reported that BP nanosheets can destroy the integrity of mitochondria and increase ROS production, which in turn activates apoptosis in human bronchial epithelial cells.[36] Moreover, evidence of BP-induced oxidative stress has been provided by *in vivo* investigations. In the liver of mice injected with BP, oxidative stress—including lipid peroxidation, reduced catalase activity, and DNA breaks—can be transiently induced by BP quantum dots but gradually recovers to normal levels.[38] In addition, BP toxicity involves ferroptosis and autophagy. A recent study reported that BP quantum dots increased m6A levels and triggered ferroptosis in lung cells.[39] BP quantum dots can also activate autophagy *via* endoplasmic reticulum stress in human bronchial epithelial cells.[40] Herein, we found that BPNPs triggered mitophagy *via* the PINK1/Parkin pathway, which, to the best of our knowledge, has never been reported before in the context of BP toxicity.

While BP-based materials demonstrate remarkable free radical scavenging capabilities due to their unique structural characteristics and electrochemical properties,[33,41] accumulating evidence reveals paradoxical cytotoxic effects across different cellular models, with oxidative stress serving as a pivotal mediator in their toxicity.[38,42−44] Mechanism investigations have elucidated that BP-induced cytotoxicity correlates with phosphate anion accumulation, which subsequently promotes lipid peroxidation and exacerbates oxidative stress.[35] This critical balance between the intrinsic antioxidant capacity and pro-oxidant activity plays crucial role in determining BP nanomaterial biocompatibility. Except the above-mentioned factors, three principal factors could modulate the intracellular behavior of BP nanomaterials: (1) Cell-type specificity: BP nanomaterials can selectively kill cancer cells, while remaining biocompatible in normal cells.[45] Further studies revealed that this is due to accelerated energy metabolism in cancer cells, which leads to acute elevation of phosphate anions and subsequently induces ROS production.[35] This metabolic vulnerability underpins their therapeutic potential while preserving normal cell viability. (2) Pathophysiological microenvironment: While BP nanosheets maintain biocompatibility under physiological conditions, their cytotoxicity becomes pronounced under oxidative stress conditions,[46] suggesting redox state-dependent toxicity modulation. (3) Dose−response effect: Previous study has demonstrated that once the dosage exceeds a certain threshold, BP-based materials could generate significant intracellular ROS and lead to DNA damage and pathological alterations.[35]

The placenta is a transient organ at the maternal−fetal interface that plays a crucial role in fetal growth. Its formation is a complex process involving the coordinated regulation of trophoblast proliferation, differentiation, and invasion into the maternal decidua.[47] Trophoblast cells constitute the main cell type of the placenta's outer layer.[14] In mice, trophoblast formation begins on GD5 when the blastocyst implants onto the uterus. The interaction between trophoblast cells and the maternal decidua is particularly important for successful placentation. Impairments in trophoblast function during the first trimester frequently result in pregnancy failure. Herein, we investigated the underlying mechanisms of BPNPs-induced reproductive toxicity using the HTR8/SVneo cell line, an extravillous trophoblast model commonly used to study trophoblast function. Our findings indicate that BPNPs exposure severely impaired trophoblast proliferation, invasion, and migration. Moreover, apoptosis was induced in a dose-dependent manner. Collectively, these effects could considerably disrupt placental development, ultimately affecting fetal growth.

Oxidative stress response has not only become an established paradigm for assessing the toxicity of various NPs[48] but it is also closely associated with the physiopathology of human pregnancy.[49] Herein, our study observed excessive ROS production in trophoblast cells following BPNPs treatment. During early pregnancy (before 10 weeks of gestation), placental tissue develops in a physiologically low-oxygen environment.[50] Then, at the end of the first trimester, there is an increase of placental metabolism and physiological oxidative status[51] to maintain and support the rapid develop-

https://doi.org/10.1021/acsnano.4c18731
ACS Nano 2025, 19, 16517−16533

ment of placenta and fetus. This renders the placenta exceptionally sensitive to BP nanoparticle-induced oxidative perturbations. This could explain the observed selective toxicity to placenta development without significant damage to other organs, reflecting tissue-specific redox homeostasis differentials.

Mitochondria are the primary source of intracellular ROS production.[52] As ROS accumulate, mitochondrial membrane permeability increases, disrupting intracellular redox homeostasis. This ultimately leads to the widespread oxidation of cellular macromolecules (lipids, proteins, DNA, *etc.*) and extensive organelle damage, including mitochondrial dysfunction. Autophagy serves as a protective mechanism that maintains cellular homeostasis by degrading damaged organelles and unnecessary proteins. Mitophagy, a specialized form of autophagy, removes damaged or nonfunctional mitochondria to reduce excessive ROS, primarily through the Parkin/PINK1 signaling pathway.[53] Herein, we present new findings showing that mitochondrial ROS levels were elevated in BPNPs-treated trophoblast cells, leading to extensive mitochondrial damage, as evidenced by accumulated fragmented mitochondria and decreased MMP. When MMP is dissipated, PINK1 accumulates on the outer mitochondrial membrane, where it recruits Parkin to impaired mitochondria.[54] Mdivi-1, a specific inhibitor of Parkin mitochondrial translocation, suppressed mitochondrial ROS production, inhibited Parkin recruitment to mitochondria, and mitigated BPNPs-induced dysfunction in HTR8 cells. Supporting these findings, *in vivo* data further demonstrated that mdivi-1 ameliorated embryonic resorption and fetal growth restriction by alleviating placental damage, suggesting that mitophagy serves as a potential therapeutic target for mitigating the adverse biological effects of BPNPs.

CONCLUSIONS

We demonstrated that gestational exposure to BPNPs with a diameter of 10−20 nm can lead to their accumulation in mouse placental tissue, resulting in adverse pregnancy outcomes. In human trophoblast, BPNPs exposure resulted in excessive mitochondrial ROS production and a decline in MMP. This triggered excessive mitophagy *via* the PINK1/Parkin pathway, subsequently inhibiting trophoblast proliferation, migration, and invasion during gestation. To the best of our knowledge, this is the first report to reveal the role of mitophagy in BP-induced cytotoxicity. However, we did not investigate the effects of varying doses or different gestational stages, and the precise mechanisms regulating mitophagy warrant further exploration.

METHODS

Animal Work. All animal procedures were conducted in compliance with the Ethical Committee of Maternal and Child Health Care Hospital of Shandong Province, affiliated with Qingdao University, under protocol number 2024−036. ICR mice were obtained from Beijing Weitonglihua and housed under a 12-h light/12-h dark cycle with free access to food and water. Female mice were mated with males at a 1:2 ratio, and the presence of a vaginal plug was designated as gestation day GD0.5. Pregnant mice were randomly assigned to one of four groups: control, BPNPs, Mdivi-1, or BPNPs +Mdivi-1. Mice in the BPNPs group received an intravenous injection of BPNPs at a concentration of 5 mg/kg on GD6.5. The mice in Mdivi-1 and BPNPs+Mdivi-1 groups received intraperitoneal injections of 25 mg/kg Mdivi-1 (HY-15886, MedChem Express) from GD6.5 to GD18.5.[19] Control group mice were administered an equal volume of saline. On GD18.5, all mice were euthanized, and placenta and fetal weights were recorded.

Preparation and Characterization of BPNPs. BPNPs were prepared using an electrochemical exfoliation method,[55] which combines electrochemical intercalation and sonication. Briefly, BP bulk (purchased from 2D Materials) was pre-expanded at a cathodic voltage of −5 V (*vs* Pt) for 30 min in an electrolyte containing 0.05 mol/L tetrabutyl ammonium dissolved in *N*,*N*-dimethylformamide.[56] The weakly entangled BP powder was then collected through filtration and redispersed in *N*-methyl-2-pyrrolidone (NMP) through sonication in an ice bath for 1 h, using a sonic tip operating at 800 W in an alternating mode (2 s on, 4 s off). The ultrasound frequency ranged between 19 and 25 kHz. To further reduce the BP flake size to the nanometer scale, the dispersion underwent an additional 6-h sonication at 300 W in an ultrasonic bath to further reduce the size of BP flake to the nanometer scale. The obtained dispersion was centrifuged at 1000 rpm for 10 min to eliminate thick BP flakes. The supernatant was then further centrifuged at 12,000 rpm for 20 min to collect the precipitate, which was rinsed three times with deionized water and resuspended in an aqueous solution for final use. The morphology of BP was examined using TEM with an FEI Titan 80−300 S/TEM operated at 200 kV. The lateral size was statistically analyzed using ImageJ, with measurements taken from 100 NPs.

Biodistribution Analysis. To visualize the biodistribution of BPNP *in vivo*, Cy5.5-labeled BPNPs were prepared as previously described.[23,26] Briefly, 0.1 mg/mL of Cy5.5 was added into the BPNP solution, followed by 4-h sonication and subsequent overnight stirring at room temperature in dark. Unbound fluorophores were removed through iterative centrifugation (12,000*g*, 15 min) and extensive washing with water until the supernatant exhibited no detectable fluorescence signal. The Cy5.5-BPNP were resuspended in sterile saline and administered *via* tail vein injection (dose: 5 mg/kg) to pregnant mice at gestational day 12.5 (GD12.5). *In vivo* imaging was performed using an IVIS Spectrum system at 6, 12, 24, 48, and 72 h postadministration. For *ex vivo* biodistribution analysis, mice were humanely euthanized *via* cervical dislocation in compliance with institutional animal ethics protocols. Major organs (heart, liver, spleen, kidneys, uterus) were surgically excised and imaged immediately. The fluorescence intensity was analyzed using Living Image 4.2.

Cell Culture and Treatments. The human trophoblast cell line HTR8/SVneo (HTR8) was purchased from the American Type Culture Collection and cultured in RPMI 1640 medium (Invitrogen, California) supplemented with 10% fetal bovine serum (FBS, GIBCO) and 1% penicillin−streptomycin antibiotics (P7630, Solarbio, China). HTR8 cells were treated with various concentrations of BPNPs for 24 h. Cells were pretreated with 10 μM Mdivi-1 (HY-15886, MCE) or 2.5 μM N-acetyl cysteine (NAC, A7250, Sigma) for 1 h before BPNPs stimulation.

Cell Viability. Cell viability was assessed using the Cell Counting Kit-8 (CCK-8) assay (CK04−100T, Solarbio, China) following the manufacturer's instructions. Briefly, HTR8 cells were seeded in a 96-well plate at a density of 6000−8000 cells per well and cultured for 24 h at 37 °C. The cells were then treated with various concentrations of BPNPs for an additional 24 h. Then, the medium was replaced with a fresh culture medium containing 10 μL of CCK-8 solution. After incubation for 2−4 h, absorbance at 450 nm was detected using a microplate reader (Norgen Biotek Corp., Canada).

EdU Assay. Cell proliferation was assessed using the EdU staining kit (C0075, Beyotime, China) following the manufacturer's instructions. Briefly, after the indicated treatments, proliferating cells were labeled with 10 μM EdU reagent for 2 h at 37 °C. The cells were then fixed with 4% paraformaldehyde (PFA) for 15 min and permeabilized with 0.3% Triton X-100 for another 15 min. After washing with PBS, cells were incubated with the Click-Reaction mix for 30 min in the dark. Hoechst 33342 (C1027, Beyotime, China) was used to counterstain the nuclei. Images were acquired and analyzed using the ImageXpress Micro Confocal High-Content Imaging System (Molecular Devices).

https://doi.org/10.1021/acsnano.4c18731
ACS Nano 2025, 19, 16517−16533

Detection of Apoptosis. Cell apoptosis was assessed using the Annexin V-fluorescein isothiocyanate (FITC)/PI apoptosis detection kit (A6030, Uelandy, China) following the manufacturer's instructions. Briefly, after the treatment, HTR8 cells were collected and stained with Annexin V-FITC and PI solution for 30 min. Then, apoptosis was analyzed using a flow cytometer (BD FACSCaliber, Germany).

Immunoblotting. Tissue and cellular proteins were extracted using RIPA lysis buffer, separated on a 10−12% SDS−PAGE gel, and transferred onto a PVDF membrane. The membrane was blocked with 5% nonfat milk in TBST buffer at room temperature for 1 h and incubated with the appropriate primary antibody at 4 °C overnight. After washing, it was then incubated with a horseradish peroxidase (HRP)-conjugated secondary antibody at room temperature for 1 h. Protein bands were visualized using an enhanced chemiluminescence detection kit (Amersham LifeScience, U.K.), and target protein expression was normalized to β-Actin. Each experiment was performed at least three times, and representative images were presented. The antibodies used herein include LC3A/B (12741, Cell Signaling Technology), Parkin (382616, ZENBIO, China), PINK (A00201−2, Boster, China), p62 (8025S, Cell Signaling Technology), TOMM20 (66777−1−1g, Proteintech, China), β-Actin (66009−1-Ig, Proteintech, China), HRP-labeled goat antimouse IgG (GB23301, Servicebio, China), and HRP-labeled goat antirabbit IgG (GB23303, Servicebio, China).

RNA Interference. HTR8 cells were cultured to 70% confluence in six-well plates before being transfected with specific interfering RNAs (siRNA) targeting human Parkin. The siRNA was incubated with Lipofectamine RNAiMAX (13778150, Life Technologies) in Opti-MEM without serum for 20 min. The scrambled RNA was used as a control. The transfection mixture was then added to the cell medium without serum, allowing the cells to undergo transfection for 6 h. Then, the cells were grown in a complete medium for 18 h prior to BPNPs stimulation. The sequences of Parkin siRNA were 5′-GCUCCAUCACUUCAGGAUUTT-3′ (sense) and 5′-AUUCCU-GAAGUGAUGGAGCTT-3′ (antisense), while the scrambled siRNA control sequences were 5′-UUCUCCGAACGUGUCACGUUU-3′ (sense) and 5′-ACGUGACACGUUCGGAGAAUU-3′ (antisense).

Mitochondrial Superoxide Assay. Mitochondrial ROS was detected using MitoSOX Red (M36007, Life Technologies). After 24 h of BPNPs treatment, HTR8 cells were washed with PBS and incubated in HBSS containing MitoSOX Red (5 μM), Mito-Tracker Green (20 nM, C1048, Beyotime), and Hoechst (C1027, Beyotime, China) for 15 min at 37 °C. The cells were then gently washed with 1× PBS and visualized using an AX R with an NSPARC confocal system (Nikon, Japan).

TEM. The ultrastructural features of HTR8 cells subjected to the indicated treatments were examined using TEM. Briefly, the cells were gently collected by centrifugation and fixed in 2.5% glutaraldehyde, followed by postfixation with 1% OsO_4 for 2 h. The samples were then dehydrated using a graded ethanol series (30, 50, 70, 80, 85, 90, 95, and 100%), infiltrated, and embedded in epoxy resin. Ultrathin sections (60−80 nm) were obtained and stained with uranyl acetate and lead citrate before imaging with a Hitachi TEM system.

Transcriptome. Total RNA was extracted from three independent cell culture experiments using TRIzol. DEGs with 2-fold or more changes between BPNPs and the control group were discriminated with an adjusted p value of 0.05 or less.

Transwell Assay. Cell invasion capacity was assessed using a Transwell assay with a Bio-Coat Matrigel Invasion Chamber (Corning). Briefly, after the indicated treatment, 1×10^5 HTR8 cells were seeded into the upper chamber precoated with 60 μL of Matrigel matrix (356234, Becton, Dickinson and Company) in 200 μL of serum-free medium. The lower chamber contained 600 μL of medium supplemented with 10% FBS. After 24 h, cells that had invaded the bottom membrane of the inset were fixed with 4% PFA, stained with 1% crystal violet for 30 min, and photographed under an inverted microscope. The number of invaded cells was quantified using ImageJ.

Wound Healing Assay. HTR8 cells were seeded in six-well plates. When confluence reached 90%, a sterile 200-μL pipet tip was used to create a scratch. Images of the scratched area were captured at 0 h under a phase-contrast microscope. Cells were then cultured in a medium containing 2.5% FBS with the indicated BPNPs treatment for 24 h, after which images were taken again to assess the scratched area. The difference in the scratched area between 0 and 24 h was measured using ImageJ, and the wound closure rate was calculated as a percentage (%) relative to the control group.

Tube Formation Assay. A precooled 96-well plate was coated with 60 μL of Matrigel (356234, Becton, Dickinson and Company) and allowed to solidify for 1 h at 37 °C. A total of 3×10^4 HTR8 cells with the indicated treatments were seeded onto the Matrigel and incubated for 3 h. The cells were then stained with 5 μM calcein acetoxymethyl ester (C2012, Beyotime, China) for 15 min. Tube formation was observed using an inverted fluorescent microscope (Nikon, Japan). The number of branch node junctions was quantified using ImageJ.

MMP Measurement. MMP was measured using the JC-1 probe (C2005, Beyotime, China). After treatment with BPNPs for 24 h, cells were incubated in a medium containing 10 μM JC-1 for 15 min. After washing with PBS, the fluorescence of JC-1 monomers and aggregates was observed using an inverted fluorescent microscope (Nikon, Japan).

Intracellular ROS Staining. 2′,7′-Dichlorofluorescin diacetate (DCFH-DA, C2938, Invitrogen, China) was used to detect intracellular ROS levels. HTR8 cells were seeded in a 96-well or 24-well plate and treated with different concentrations of BPNPs for 24 h. Then, the cells were stained with 10 μM DCFH-DA for 30 min. To quantify the fluorescence, the cells were trypsinized, washed, and resuspended in 1× PBS and analyzed on flow cytometry (BD BIOSciences, Germany) with an excitation wavelength of 488 nm and an emission wavelength of 530 nm. The mean fluorescence intensity was quantified and analyzed using FlowJo.

SOD and MDA Assay. SOD and MDA assays were performed according to the manufacturer's instructions using the following kits: Total Superoxide Dismutase Assay Kit (S0101S, Beyotime, China), Lipid Peroxidation MDA Assay Kit (S0131S, Beyotime, China).

Hyperspectral-Enhanced Dark-Field Microscopy. Harvested placentas were fixed in formalin, embedded in paraffin, and sectioned at 3 μm. The sections were deparaffinized by washing twice in xylene, rehydrated through a graded ethanol series (100, 95, 85, 75%, 10 min each), and then washed in 1× PBS before being mounted with neutral resin. A CytoViva Enhanced Darkfield Hyperspectral Microscope (CytoViva, Inc., Auburn, AL) was used to identify the localization of BPNPs within placental tissues. Spectral libraries of BPNPs were manually generated from hyperspectral images of exposed placenta, and the Filter Spectral Library function was applied to eliminate false positives by removing spectra similar to those of blank control (nonexposed placenta). The spectral libraries of BPNPs were then analyzed using the spectral angle mapper algorithm for matching with exposed placenta hyperspectral imaging. Images were captured at 60× magnification with an oil objective, and data were processed using ENVI 4.8 (CytoViva, Inc., Auburn, AL).

Statistical Analysis. Statistical significance was evaluated using one-way analysis of variance in GraphPad Prism 8.0. Data were presented as mean ± standard error of the mean from at least three biological replicates. Statistical significance was set as * for $p \leq 0.05$, ** for $p \leq 0.01$, and *** for $p \leq 0.001$.

ASSOCIATED CONTENT

Data Availability Statement

The data sets used and/or analyzed during the current study are available from the corresponding author on reasonable request.

Supporting Information

The Supporting Information is available free of charge at https://pubs.acs.org/doi/10.1021/acsnano.4c18731.

https://doi.org/10.1021/acsnano.4c18731
ACS Nano 2025, 19, 16517−16533

Histological examination of the main organs in BPNPs-treated mice; the redox state of BPNPs-treated mouse placenta; immunofluorescence staining of Parkin and TOMM20 in mouse placenta; NAC rescued BPNPs-caused cell function impairment; Mdivi-1 mitigated the mitochondrial damages in trophoblasts (PDF)

AUTHOR INFORMATION

Corresponding Authors

Xietong Wang − *Key Laboratory of Maternal & Fetal Medicine of National Health Commission of China, Shandong Provincial Maternal and Child Health Care Hospital Affiliated to Qingdao University, Jinan 250014, China*; Email: xietong789656@163.com

Meihua Zhang − *Key Laboratory of Maternal & Fetal Medicine of National Health Commission of China, Shandong Provincial Maternal and Child Health Care Hospital Affiliated to Qingdao University, Jinan 250014, China*; orcid.org/0000-0002-6821-1168; Email: meihua2013@163.com

Authors

Changqing Zhang − *Key Laboratory of Maternal & Fetal Medicine of National Health Commission of China, Shandong Provincial Maternal and Child Health Care Hospital Affiliated to Qingdao University, Jinan 250014, China*

Li Xiao − *Key Laboratory of Maternal & Fetal Medicine of National Health Commission of China, Shandong Provincial Maternal and Child Health Care Hospital Affiliated to Qingdao University, Jinan 250014, China*

Zhenya Fang − *Key Laboratory of Maternal & Fetal Medicine of National Health Commission of China, Shandong Provincial Maternal and Child Health Care Hospital Affiliated to Qingdao University, Jinan 250014, China*

Shuxian Li − *Key Laboratory of Maternal & Fetal Medicine of National Health Commission of China, Shandong Provincial Maternal and Child Health Care Hospital Affiliated to Qingdao University, Jinan 250014, China*

Chao Fan − *Key Laboratory of Maternal & Fetal Medicine of National Health Commission of China, Shandong Provincial Maternal and Child Health Care Hospital Affiliated to Qingdao University, Jinan 250014, China*

Ruolan You − *School of Public Health, Shandong Second Medical University, Weifang 261053, China*

Chunying Wang − *Key Laboratory of Maternal & Fetal Medicine of National Health Commission of China, Shandong Provincial Maternal and Child Health Care Hospital Affiliated to Qingdao University, Jinan 250014, China*

Anna Li − *Key Laboratory of Maternal & Fetal Medicine of National Health Commission of China, Shandong Provincial Maternal and Child Health Care Hospital Affiliated to Qingdao University, Jinan 250014, China*

Complete contact information is available at: https://pubs.acs.org/10.1021/acsnano.4c18731

Author Contributions

C.Z.: Conceptualization, data curation, formal analysis, investigation, writing—original draft. L.X.: Methodology, resources. S.L.: methodology, software. R.Y.: Data curation, investigation, validation. C.W.: Data curation, investigation. C.F.: Methodology, software. A.L.: Methodology, resources. Z.F.: Resources, software. M.Z.: Project administration, supervision, resources. X.W.: Project administration, supervision, resources, funding acquisition.

Funding

This work was supported by the Project of China Maternal and Child Health Association, 2023CAMCHS003A06 and Shandong Provincial Medical and Health Technology Programme, 202305021575.

Notes

The authors declare no competing financial interest.

Ethics approval All animal work was performed in accordance with the Ethical Committee of Maternal and Child Health Care Hospital of Shandong Province Affiliated to Qingdao University under protocol number of 2024−036.

ACKNOWLEDGMENTS

We would like to thank Prof. Li Jing (Beihang University) for technical assistance.

REFERENCES

(1) Liu, H.; Neal, A. T.; Zhu, Z.; Luo, Z.; Xu, X.; Tomanek, D.; Ye, P. D. Phosphorene: an unexplored 2D semiconductor with a high hole mobility. *ACS Nano* **2014**, *8* (4), 4033−4041.

(2) Kim, H.; Uddin, S. Z.; Lien, D. H.; Yeh, M.; Azar, N. S.; Balendhran, S.; Kim, T.; Gupta, N.; Rho, Y.; Grigoropoulos, C. P.; Crozier, K. B.; Javey, A. Actively variable-spectrum optoelectronics with black phosphorus. *Nature* **2021**, *596* (7871), 232−237.

(3) Xia, F.; Wang, H.; Jia, Y. Rediscovering black phosphorus as an anisotropic layered material for optoelectronics and electronics. *Nat. Commun.* **2014**, *5*, No. 4458.

(4) Zhou, L.; Liu, C.; Sun, Z.; Mao, H.; Zhang, L.; Yu, X.; Zhao, J.; Chen, X. Black phosphorus based fiber optic biosensor for ultrasensitive cancer diagnosis. *Biosens. Bioelectron.* **2019**, *137*, 140−147.

(5) Sun, Y.; He, W.; Jiang, C.; Li, J.; Liu, J.; Liu, M. Wearable Biodevices Based on Two-Dimensional Materials: From Flexible Sensors to Smart Integrated Systems. *Nano-Micro Lett.* **2025**, *17* (1), No. 109.

(6) Wang, Z.; Liu, Z.; Su, C.; Yang, B.; Fei, X.; Li, Y.; Hou, Y.; Zhao, H.; Guo, Y.; Zhuang, Z.; Zhong, H.; Guo, Z. Biodegradable Black Phosphorus-based Nanomaterials in Biomedicine: Theranostic Applications. *Curr. Med. Chem.* **2019**, *26* (10), 1788−1805.

(7) Sun, Z.; Xie, H.; Tang, S.; Yu, X. F.; Guo, Z.; Shao, J.; Zhang, H.; Huang, H.; Wang, H.; Chu, P. K. Ultrasmall Black Phosphorus Quantum Dots: Synthesis and Use as Photothermal Agents. *Angew. Chem., Int. Ed.* **2015**, *54* (39), 11526−11530.

(8) Wang, H.; Yang, X.; Shao, W.; Chen, S.; Xie, J.; Zhang, X.; Wang, J.; Xie, Y. Ultrathin Black Phosphorus Nanosheets for Efficient Singlet Oxygen Generation. *J. Am. Chem. Soc.* **2015**, *137* (35), 11376−11382.

(9) Song, S. J.; Shin, Y. C.; Lee, H. U.; Kim, B.; Han, D. W.; Lim, D. Dose- and Time-Dependent Cytotoxicity of Layered Black Phosphorus in Fibroblastic Cells. *Nanomaterials* **2018**, *8* (6), No. 408.

(10) Song, S. J.; Raja, I. S.; Lee, Y. B.; Kang, M. S.; Seo, H. J.; Lee, H. U.; Han, D. W. Comparison of cytotoxicity of black phosphorus nanosheets in different types of fibroblasts. *Biomater. Res.* **2019**, *23*, No. 23.

(11) Zhang, X.; Zhang, Z.; Zhang, S.; Li, D.; Ma, W.; Ma, C.; Wu, F.; Zhao, Q.; Yan, Q.; Xing, B. Size Effect on the Cytotoxicity of Layered Black Phosphorus and Underlying Mechanisms. *Small* **2017**, *13* (32), No. 1701210.

(12) Yang, X.; Liang, J.; Wu, Q.; Li, M.; Shan, W.; Zeng, L.; Yao, L.; Liang, Y.; Wang, C.; Gao, J.; Guo, Y.; Liu, Y.; Liu, R.; Luo, Q.; Zhou, Q.; Qu, G.; Jiang, G. Developmental Toxicity of Few-Layered Black

Phosphorus toward Zebrafish. *Environ. Sci. Technol.* **2021**, *55* (2), 1134−1144.
(13) Sibley, C. P. Treating the dysfunctional placenta. *J. Endocrinol.* **2017**, *234* (2), R81−R97.
(14) Staud, F.; Karahoda, R. Trophoblast: The central unit of fetal growth, protection and programming. *Int. J. Biochem. Cell Biol.* **2018**, *105*, 35−40.
(15) Strack, R. A clearer view of mitophagy. *Nat. Methods* **2020**, *17* (7), No. 656.
(16) Saito, S.; Nakashima, A. A review of the mechanism for poor placentation in early-onset preeclampsia: the role of autophagy in trophoblast invasion and vascular remodeling. *J. Reprod. Immunol.* **2014**, *101−102*, 80−88.
(17) Gao, L.; Qi, H. B.; Kamana, K. C.; Zhang, X. M.; Zhang, H.; Baker, P. N. Excessive autophagy induces the failure of trophoblast invasion and vasculature: possible relevance to the pathogenesis of preeclampsia. *J. Hypertens.* **2015**, *33* (1), 106−117.
(18) Sferruzzi-Perri, A. N.; Higgins, J. S.; Vaughan, O. R.; Murray, A. J.; Fowden, A. L. Placental mitochondria adapt developmentally and in response to hypoxia to support fetal growth. *Proc. Natl. Acad. Sci. U.S.A.* **2019**, *116* (5), 1621−1626.
(19) Zhu, H. L.; Dai, L. M.; Xiong, Y. W.; Shi, X. T.; Liu, W. B.; Fu, Y. T.; Zhou, G. X.; Zhang, S.; Gao, L.; Zhang, C.; Zhao, L. L.; Xu, X. F.; Huang, Y. C.; Xu, D. X.; Wang, H. Gestational exposure to environmental cadmium induces placental apoptosis and fetal growth restriction via Parkin-modulated MCL-1 degradation. *J. Hazard. Mater.* **2022**, *424*, No. 127268.
(20) Chen, Z.; Geng, Y.; Gao, R.; Zhong, H.; Chen, J.; Mu, X.; Chen, X.; Zhang, Y.; Li, F.; He, J. Maternal exposure to CeO(2)NPs derails placental development through trophoblast dysfunction mediated by excessive autophagy activation. *J. Nanobiotechnol.* **2022**, *20* (1), No. 131.
(21) Zhu, H. L.; Shi, X. T.; Xu, X. F.; Xiong, Y. W.; Yi, S. J.; Zhou, G. X.; Liu, W. B.; Huang, M. M.; Gao, L.; Zhang, C.; Zhao, L. L.; Xu, D. X.; Wang, H. Environmental cadmium exposure induces fetal growth restriction via triggering PERK-regulated mitophagy in placental trophoblasts. *Environ. Int.* **2021**, *147*, No. 106319.
(22) Xiong, Y. W.; Xu, X. F.; Zhu, H. L.; Cao, X. L.; Yi, S. J.; Shi, X. T.; Zhu, K. H.; Nan, Y.; Zhao, L. L.; Zhang, C.; Gao, L.; Chen, Y. H.; Xu, D. X.; Wang, H. Environmental exposure to cadmium impairs fetal growth and placental angiogenesis via GCN-2-mediated mitochondrial stress. *J. Hazard. Mater.* **2021**, *401*, No. 123438.
(23) Geng, S.; Pan, T.; Zhou, W.; Cui, H.; Wu, L.; Li, Z.; Chu, P. K.; Yu, X. F. Bioactive phospho-therapy with black phosphorus for in vivo tumor suppression. *Theranostics* **2020**, *10* (11), 4720−4736.
(24) Yang, X.; Wang, D.; Shi, Y.; Zou, J.; Zhao, Q.; Zhang, Q.; Huang, W.; Shao, J.; Xie, X.; Dong, X. Black Phosphorus Nanosheets Immobilizing Ce6 for Imaging-Guided Photothermal/Photodynamic Cancer Therapy. *ACS Appl. Mater. Interfaces* **2018**, *10* (15), 12431−12440.
(25) Shao, J.; Xie, H.; Huang, H.; Li, Z.; Sun, Z.; Xu, Y.; Xiao, Q.; Yu, X. F.; Zhao, Y.; Zhang, H.; Wang, H.; Chu, P. K. Biodegradable black phosphorus-based nanospheres for in vivo photothermal cancer therapy. *Nat. Commun.* **2016**, *7*, No. 12967.
(26) Geng, S.; Zhang, X.; Luo, T.; Jiang, M.; Chu, C.; Wu, L.; Gong, P.; Zhou, W. Combined chemotherapy based on bioactive black phosphorus for pancreatic cancer therapy. *J. Controlled Release* **2023**, *354*, 889−901.
(27) Chen, W.; Ouyang, J.; Liu, H.; Chen, M.; Zeng, K.; Sheng, J.; Liu, Z.; Han, Y.; Wang, L.; Li, J.; Deng, L.; Liu, Y. N.; Guo, S. Black Phosphorus Nanosheet-Based Drug Delivery System for Synergistic Photodynamic/Photothermal/Chemotherapy of Cancer *Adv. Mater.* 2017; Vol. *29* 5 DOI: 10.1002/adma.201603864.
(28) Latiff, N. M.; Teo, W. Z.; Sofer, Z.; Fisher, A. C.; Pumera, M. The Cytotoxicity of Layered Black Phosphorus. *Chemistry* **2015**, *21* (40), 13991−13995.
(29) Qiu, M.; Wang, D.; Liang, W.; Liu, L.; Zhang, Y.; Chen, X.; Sang, D. K.; Xing, C.; Li, Z.; Dong, B.; Xing, F.; Fan, D.; Bao, S.; Zhang, H.; Cao, Y. Novel concept of the smart NIR-light-controlled drug release of black phosphorus nanostructure for cancer therapy. *Proc. Natl. Acad. Sci. U.S.A.* **2018**, *115* (3), 501−506.
(30) Shao, J.; Ruan, C.; Xie, H.; Li, Z.; Wang, H.; Chu, P. K.; Yu, X. F. Black-Phosphorus-Incorporated Hydrogel as a Sprayable and Biodegradable Photothermal Platform for Postsurgical Treatment of Cancer. *Adv. Sci.* **2018**, *5* (5), No. 1700848.
(31) He, C.; Ruan, F.; Jiang, S.; Zeng, J.; Yin, H.; Liu, R.; Zhang, Y.; Huang, L.; Wang, C.; Ma, S.; Zuo, Z. Black Phosphorus Quantum Dots Cause Nephrotoxicity in Organoids, Mice, and Human Cells. *Small* **2020**, *16* (22), No. e2001371.
(32) Jin, L.; Hu, P.; Wang, Y.; Wu, L.; Qin, K.; Cheng, H.; Wang, S.; Pan, B.; Xin, H.; Zhang, W.; Wang, X. Fast-Acting Black-Phosphorus-Assisted Depression Therapy with Low Toxicity. *Adv. Mater.* **2020**, *32* (2), No. e1906050.
(33) Hou, J.; Wang, H.; Ge, Z.; Zuo, T.; Chen, Q.; Liu, X.; Mou, S.; Fan, C.; Xie, Y.; Wang, L. Treating Acute Kidney Injury with Antioxidative Black Phosphorus Nanosheets. *Nano Lett.* **2020**, *20* (2), 1447−1454.
(34) Sun, C.; Wen, L.; Zeng, J.; Wang, Y.; Sun, Q.; Deng, L.; Zhao, C.; Li, Z. One-pot solventless preparation of PEGylated black phosphorus nanoparticles for photoacoustic imaging and photothermal therapy of cancer. *Biomaterials* **2016**, *91*, 81−89.
(35) Kong, N.; Ji, X.; Wang, J.; Sun, X.; Chen, G.; Fan, T.; Liang, W.; Zhang, H.; Xie, A.; Farokhzad, O. C.; Tao, W. ROS-Mediated Selective Killing Effect of Black Phosphorus: Mechanistic Understanding and Its Guidance for Safe Biomedical Applications. *Nano Lett.* **2020**, *20* (5), 3943−3955.
(36) Sun, Y.; Fan, S.; Fan, S.; Li, C.; Shang, Z.; Gu, M.; Liang, S.; Tian, X. In Vitro and In Vivo Toxicity of Black Phosphorus Nanosheets. *J. Nanosci. Nanotechnol.* **2020**, *20* (2), 659−667.
(37) Wang, Z.; Zhang, C.; Huang, F.; Liu, X.; Wang, Z.; Yan, B. Breakthrough of ZrO(2) nanoparticles into fetal brains depends on developmental stage of maternal placental barrier and fetal blood-brain-barrier. *J. Hazard. Mater.* **2021**, *402*, No. 123563.
(38) Mu, X.; Wang, J. Y.; Bai, X.; Xu, F.; Liu, H.; Yang, J.; Jing, Y.; Liu, L.; Xue, X.; Dai, H.; Liu, Q.; Sun, Y. M.; Liu, C.; Zhang, X. D. Black Phosphorus Quantum Dot Induced Oxidative Stress and Toxicity in Living Cells and Mice. *ACS Appl. Mater. Interfaces* **2017**, *9* (24), 20399−20409.
(39) Ruan, F.; Zeng, J.; Yin, H.; Jiang, S.; Cao, X.; Zheng, N.; Han, C.; Zhang, C.; Zuo, Z.; He, C. RNA m6A Modification Alteration by Black Phosphorus Quantum Dots Regulates Cell Ferroptosis: Implications for Nanotoxicological Assessment. *Small Methods* **2021**, *5* (3), No. e2001045.
(40) Wang, L.; Lin, M.; Hou, X.; Dou, L.; Huang, Z.; Liu, R.; Zhang, J.; Cai, C.; Chen, C.; Liu, Y.; Wang, D.; Guo, D.; An, R.; Wei, L.; Yao, Y.; Zhang, Y. Black phosphorus quantum dots induce autophagy and apoptosis of human bronchial epithelial cells via endoplasmic reticulum stress. *Chemosphere* **2023**, *327*, No. 138463.
(41) Zhang, J.; Han, S.; Zhao, Z.; Zhou, C.; Chen, H.; Hou, J.; Wu, J. Ultrasmall Black Phosphorus Quantum Dots with Robust Antioxidative Properties for Acute Kidney and Liver Injury Therapy. *Small* **2025**, *21* (1), No. e2407543.
(42) Dong, H.; Wen, Y.; Lin, J.; Zhuang, X.; Xian, R.; Li, P.; Li, S. Cytotoxicity Induced by Black Phosphorus Nanosheets in Vascular Endothelial Cells via Oxidative Stress and Apoptosis Activation. *J. Funct. Biomater.* **2023**, *14* (5), No. 284.
(43) Zhong, Y.; Lin, Y.; Chen, Y.; Chen, G.; Zhang, J.; Li, L.; Huang, A.; Zhang, L.; Ma, Y.; Xie, Z. Y.; Liao, Q. Black Phosphorus Nanosheets Induced Oxidative Stress In Vitro and Targeted Photothermal Antitumor Therapy. *ACS Appl. Bio Mater.* **2021**, *4* (2), 1704−1719.
(44) Zhang, B.; Xing, Y.; Guo, Y.; Jin, S.; Shao, X.; Fan, J.; Zhang, C.; Wang, Y. Protective Role of Melatonin against Liver Toxicity from Black Phosphorus Nanosheets via Oxidative Stress and Pyroptosis. *ACS Omega* **2024**, *9* (47), 46891−46903.
(45) Zhou, W.; Pan, T.; Cui, H.; Zhao, Z.; Chu, P. K.; Yu, X. F. Black Phosphorus: Bioactive Nanomaterials with Inherent and

Selective Chemotherapeutic Effects. *Angew. Chem., Int. Ed.* **2019**, *58* (3), 769−774.
(46) Fan, Z.; Wu, S.; An, Z.; Wang, Y.; Xu, B.; Wang, X.; Xu, Y.; Li, H.; Duan, G.; Zhang, S.; Tian, X. Unraveling the stress-induced toxicity of black phosphorus nanosheets and the underlying mechanism. *Colloid Interface Sci. Commun.* **2024**, *62*, No. 100802.
(47) Hemberger, M.; Hanna, C. W.; Dean, W. Mechanisms of early placental development in mouse and humans. *Nat. Rev. Genet.* **2020**, *21* (1), 27−43.
(48) Nel, A.; Xia, T.; Madler, L.; Li, N. Toxic potential of materials at the nanolevel. *Science* **2006**, *311* (5761), 622−627.
(49) Chiarello, D. I.; Abad, C.; Rojas, D.; Toledo, F.; Vazquez, C. M.; Mate, A.; Sobrevia, L.; Marin, R. Oxidative stress: Normal pregnancy versus preeclampsia. *Biochim. Biophys. Acta, Mol. Basis Dis.* **2020**, *1866* (2), No. 165354.
(50) Fisher, J. J.; Bartho, L. A.; Perkins, A. V.; Holland, O. J. Placental mitochondria and reactive oxygen species in the physiology and pathophysiology of pregnancy. *Clin. Exp. Pharmacol. Physiol.* **2020**, *47* (1), 176−184.
(51) Guerby, P.; Tasta, O.; Swiader, A.; Pont, F.; Bujold, E.; Parant, O.; Vayssiere, C.; Salvayre, R.; Negre-Salvayre, A. Role of oxidative stress in the dysfunction of the placental endothelial nitric oxide synthase in preeclampsia. *Redox Biol.* **2021**, *40*, No. 101861.
(52) Hernansanz-Agustín, P.; Enriquez, J. A. Generation of Reactive Oxygen Species by Mitochondria. *Antioxidants* **2021**, *10* (3), No. 415.
(53) Katayama, H.; Hama, H.; Nagasawa, K.; Kurokawa, H.; Sugiyama, M.; Ando, R.; Funata, M.; Yoshida, N.; Homma, M.; Nishimura, T.; Takahashi, M.; Ishida, Y.; Hioki, H.; Tsujihata, Y.; Miyawaki, A. Visualizing and Modulating Mitophagy for Therapeutic Studies of Neurodegeneration. *Cell* **2020**, *181* (5), 1176−1187 e16.
(54) Jin, S. M.; Lazarou, M.; Wang, C.; Kane, L. A.; Narendra, D. P.; Youle, R. J. Mitochondrial membrane potential regulates PINK1 import and proteolytic destabilization by PARL. *J. Cell Biol.* **2010**, *191* (5), 933−942.
(55) Li, J.; Chen, C.; Liu, S.; Lu, J.; Goh, W. P.; Fang, H.; Qiu, Z.; Tian, B.; Chen, Z.; Yao, C.; Liu, W.; Yan, H.; Yu, Y.; Wang, D.; Wang, Y.; Lin, M.; Su, C.; Lu, J. Ultrafast Electrochemical Expansion of Black Phosphorus toward High-Yield Synthesis of Few-Layer Phosphorene. *Chem. Mater.* **2018**, *30*, 2742−2749.
(56) Li, J.; Song, P.; Zhao, J.; Vaklinova, K.; Zhao, X.; Li, Z.; Qiu, Z.; Wang, Z.; Lin, L.; Zhao, M.; Herng, T. S.; Zuo, Y.; Jonhson, W.; Yu, W.; Hai, X.; Lyu, P.; Xu, H.; Yang, H.; Chen, C.; Pennycook, S. J.; Ding, J.; Teng, J.; Castro Neto, A. H.; Novoselov, K. S.; Lu, J. Printable two-dimensional superconducting monolayers. *Nat. Mater.* **2021**, *20* (2), 181−187.

https://doi.org/10.1021/acsnano.4c18731
ACS Nano 2025, 19, 16517−16533